energies

MDPI

Article

The Wave-to-Wire Energy Conversion Process for a Fixed U-OWC Device

Luana Gurnari [1], Pasquale G. F. Filianoti [1,*], Marco Torresi [2] and Sergio M. Camporeale [2]

[1] Department of Civil, Energy, Environmental and Material Engineering (DICEAM), University Mediterranea of Reggio Calabria Via Graziella, 89122 Reggio Calabria, Italy; luana.gurnari@unirc.it

[2] Department of Mechanics, Mathematics and Management (DMMM), Politecnico di Bari, Bari, via Orabona 4, 70125 Bari, Italy; marco.torresi@poliba.it (M.T.); sergio.camporeale@poliba.it (S.M.C.)

* Correspondence: filianoti@unirc.it; Tel.: +39-338-970-6172

Received: 8 November 2019; Accepted: 3 January 2020; Published: 6 January 2020

Abstract: Oscillating water column (OWC) devices, either fixed or floating, are the most common wave energy converter (WEC) devices. In this work, the fluid dynamic interaction between waves and a U-shaped OWC breakwater embedding a Wells turbine has been investigated through unsteady Computational Fluid Dynamic (CFD) simulations. The full-scale plant installed in the harbor of Civitavecchia (Italy) was numerically modeled. A two-dimensional domain was adopted to simulate the unsteady flow, both outside and inside the U-OWC device, including the air chamber and the oscillating flow inside the conduit hosting the Wells turbine. For the numerical simulation of the damping effect induced by the Wells turbine connected to the air chamber, a porous medium was placed in the computational domain, representing the conduit hosting the turbine. Several simulations were carried out considering periodic waves with different periods and amplitudes, getting a deep insight into the energy conversion process from wave to the turbine power output. For this purpose, the three main steps of the overall energy conversion process have been examined. Firstly, from the wave power to the power of the water oscillating flow inside the U-duct. Secondly, from the power of the oscillating water flow to the air pneumatic power. Finally, from the air pneumatic power to the Wells turbine power output. Results show that the U-OWC can capture up to 66% of the incoming wave power, in the case of a wave period close to the eigenperiod of the plant. However, only two-thirds of the captured energy flux is available to the turbine, being partially dissipated due to the losses in the U-duct and the air chamber. Finally, the overall time-average turbine power output is evaluated showing that it is strongly influenced by a suitable choice of the turbine characteristics (mainly geometry and rotational speed).

Keywords: wave energy converter; oscillating water column; CFD; resonance condition; porous medium; wells turbine; energy conversion chain

1. Introduction

Oceans and seas can be a fundamental renewable source of energy, considering that they cover almost two-thirds of the Earth's surface. Ocean energy has great potential, even though harnessing this resource is more difficult than it seems. The main forms of ocean energy are waves, tides, marine currents, salinity, and temperature gradients. Among all of these, the most mature technologies are currently wave and tidal energies. Many different technical concepts for extracting wave energy are presently under study and development [1–4]. One of the most promising technologies refers to oscillating water column (OWC) devices (see, e.g., [5,6]), that can be either integrated inside a breakwater, in a near-shore configuration, like in the cases of both Civitavecchia's harbour [7] and the Mutriku's harbour [8,9] or arranged as a floating device [10]. In general, an OWC device consists

of a chamber that is partially submerged in the seawater, with an air column trapped above a water column inside. The wall of the chamber, which is in front of the sea, presents a big vertical opening. Waves enter through this opening and determine the oscillation of the water surface in the chamber. On the roof of the chamber, there is a conduit connecting it to the atmosphere, and containing the power take-off (PTO) system. The incoming waves cause the water column in the chamber to compress and expand the air pocket inside it, and hence cause the inhalation and exhalation of air through the conduit. This oscillating flow drives the PTO system, which is actually a self-rectifying turbine, e.g., either a Wells turbine [10] or an impulse turbine [11]. U-OWC devices ([12,13]) belong to the family of OWCs, with some modifications with respect to conventional ones. They are caisson breakwaters in reinforced concrete embodying an OWC with an additional vertical duct on the wave-beaten side. The vertical duct is actually one of the two branches of the U-duct, the other one being the chamber. Like a standard OWC, the air chamber is connected with the atmosphere through a conduit that hosts the PTO system. To exploit a natural resonance with sea waves, the various parts of the plant have to be designed to obtain an eigenperiod of the oscillations of the free water surface inside the chamber close to the incident wave period of the wave train giving the highest energy contribution during the year. The parts to be designed (see Figure 1) are the width s, and length l, of the vertical duct, the width b, and height c, of the chamber, and the diameter D, of the air conduit [12]. When a U-OWC device works under resonance conditions, it achieves a very large absorption of the incident wave energy. A maximum absorption of 60% of the incident wave energy has been registered during the experiments carried out on a small-scale device placed in the natural laboratory of Reggio Calabria (Italy) [14]. Recently, U-OWC devices have been installed in the harbor of Civitavecchia (Italy), located in the Tyrrhenian Sea [7]. The U-OWCs were located in the area close to the harbor entrance and allowed the creation of a novel basin into the port area.

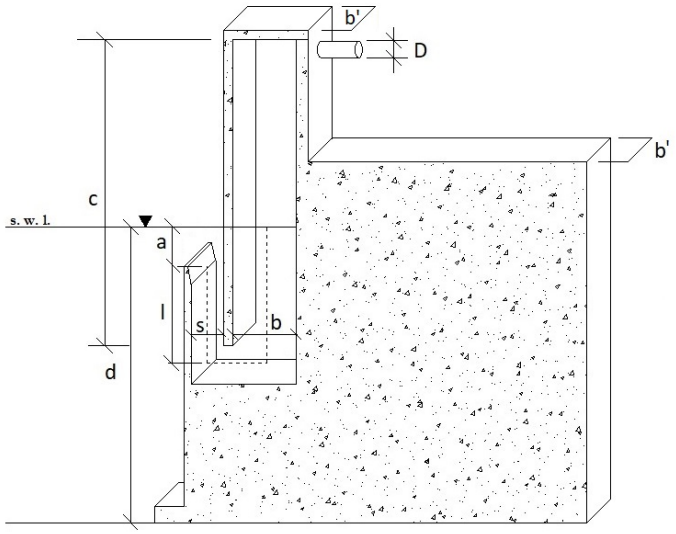

Figure 1. Vertical cross section of the caisson breakwater installed at Civitavecchia's harbour. Design adapted from [7].

Numerical one-dimensional models were developed by Boccotti in [15] and validated against small scale experiments in [16,17]. Such models, with some minor modifications, were applied by Arena et al. [7] to their full-scale U-OWC system to verify their capability of predicting the overall energy performance. However, one-dimensional models are unable to give an insight of the different hydrodynamic processes that occur in the proximity of, and inside the U-OWC system. To overcome the intrinsic limits of these one-dimensional models, a numerical approach based on CFD simulations has been proposed by the authors [18,19] and by others (e.g., [20–23]). The performance of an OWC device under a range of wavelengths for different wave steepness was analyzed by Kamat et al. [21]

by means of CFD simulations. At lower wave steepness, the effect of wave steepness values on the efficiency of the device was found to be small, but a large reduction in performance was found in the presence of steep non-linear waves. However, to investigate the overall energy conversion process, the simulations of the U-OWC device must include the characteristics of the PTO system. As it is well known, the PTO acts as a damping term in the airflow motion of an OWC excited by the incident waves (e.g., [24]). To optimize the overall efficiency of the wave energy converter (WEC) device, it must be tuned into the plant (and consequentially the PTO system) to enter in resonance with the most energetic waves of the location. To this aim, numerical modeling is useful to carry out an evaluation of the performance of the OWC operating under different values of the PTO damping (modified by changing its rotational speed), and for different incoming waves. In this work, the computational domain includes a wave flume which is 1 km long by 30 m deep and contains the U-OWC breakwater with its plenum chamber and the conduit hosting the Wells turbine. In this way, we are able to take into account all the energy conversions from waves (generated by means of a piston-type wavemaker) to the power take-off (simulated by means of momentum and energy source terms introduced with a porous medium inside the conduit), similarly to other wave-to-wire models, such as [25–28]. In order to take into account the Wells turbine effect on the fluid dynamic behavior of the air and water flow inside the WEC device in the CFD simulations, without determining a significant increase of the computational cost, a porous medium was introduced in the air conduit, giving a pressure drop linearly dependent on the flow rate, according to the Wells turbine characteristic curve. The use of a porous medium was firstly used by the authors in other applications (e.g., see [29]), and opportunely adapted here. Several examples of a similar approach can be found in various publications. The use of porous media theory to develop a numerical model of the PTO damping effect was explored by Didier et al. [30], by means of a relationship between the air pressure in the chamber and the airflow velocity across the turbine. The numerical results were validated comparing them with the experimental results collected from a physical model. In that physical model, the turbine damping effect was simulated by a piece of a porous membrane (textile) placed on the top of the cylinder. Moreover, the optimization of the turbine induced damping on an OWC device using a CFD model was studied by Lopez et al. [31], after validating the model with data from physical model tests. In both the physical and the CFD models, the turbine damping was modeled by carefully designing the area of the orifice at the top of the OWC chamber.

The advantage of using the porous medium is that we correctly take into account the linear characteristic curve of the Wells turbine, rather than approximating it as an orifice which has a parabolic characteristic curve, as it is usually done by many authors [31–33]. This paper continues with the description of the numerical experiment (in terms of the computational domain, governing equations, and PTO model) in Section 2. The fluid dynamic analysis is carried out in Section 3, describing the wave field evolution inside the flume. Then, in Section 4 the energetic analysis from the wavemaker to the absorber was described. Furthermore, the attention goes to the captured energy, and finally to the conversion of this energy into available power thanks to the power take-off.

2. The Numerical Experiment

2.1. Layout of the Numerical Domain

In order to numerically investigate the interaction between waves and the breakwater, we set up a two-dimensional numerical wave flume, with a piston-type wavemaker placed on the left side and the U-OWC breakwater, on the right side (see Figure 2). The wave flume is 1 km long and 30 m deep. This relevant length of the flume allows several wavelengths (at least 10) to be contained, between the wavemaker and the U-OWC breakwater. This distance is wide enough to investigate the unsteady wave field propagating from the U-OWC towards the wavemaker. The U-OWC device under consideration is a schematic reproduction of the plant installed at the Civitavecchia's harbor (Italy) in the Tyrrhenian Sea. The widths of both the duct and the internal chamber are 1.6 m and

3.2 m, respectively; the length of the duct is 7.0 m, the height of the chamber over the mean water level is 9.4 m. The internal chambers of each caisson breakwater are independent from each other, with a horizontal section $b \times b'$ equal to 3.2 m $\times$ 3.87 m. The still water depth was set at 15.0 m, and the outer opening of the plant is 2.0 m below the still water level. Assuming that the waves are moving perpendicularly to the OWC, a two-dimensional CFD simulation is carried out, to reduce the computational effort with respect to a fully three-dimensional simulation. Figure 2 also shows the conduit that hosts the porous medium, that is able to reproduce the pressure drops across the turbine for the CFD simulations.

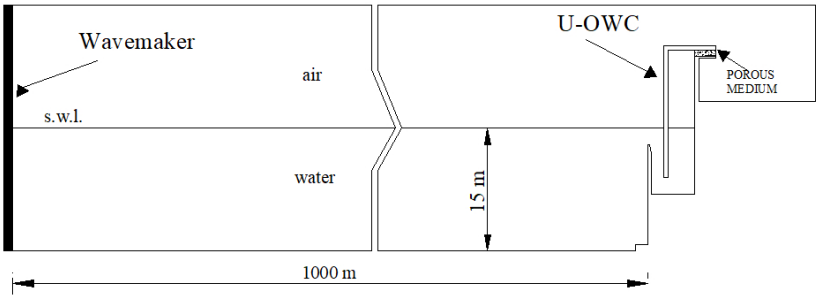

Figure 2. Sketch of the numerical wave flume (measures are in meters).

The spatial discretization of the computational domain (see Figure 3) has been portioned according to a multi-block scheme, adopting structured rectangular elements and triangular elements. In other words, we used rectangular elements along the flume, which were thinner near to the free surface displacement, to achieve a better resolution of the water surface, whereas, near the contour of the U-OWC device, we used triangular elements to guarantee a slow transition between the mesh size in the overall domain and the mesh size (which is smaller) inside the plant, where rectangular elements were used again. The mesh has approximately 300,000 cells. The mesh metric information allows the mesh quality to be evaluated. The most common quality indexes are the orthogonal quality, the skewness coefficient and the aspect ratio. In this mesh, the minimum orthogonal quality is 0.49, which is a medium value considering that the orthogonal quality ranges from 0 to 1. According to the definition of the skewness, a value of 0 indicates an equilateral cell (the best quality), and a value of 1 indicates a completely degenerated cell. The maximum skewness is about 0.29. The aspect ratio of either a face or a cell is the ratio of the longest edge length to the shortest one. The best possible result (equal to one) is achieved by both squares and equilateral triangles. In this work, the maximum aspect ratio of the spatial discretization is 2.0. Moreover, the mesh has been refined across the free water surface, in order to accurately simulate the wave elevation.

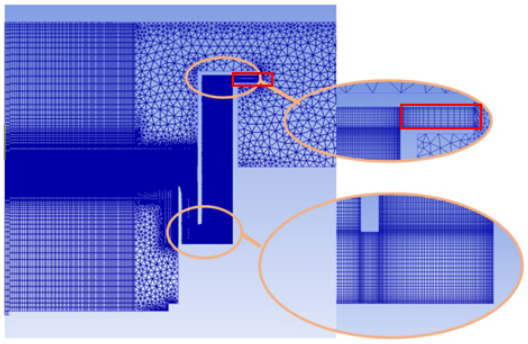

Figure 3. The spatial discretization of the computational domain. The conduit contoured by a red rectangle is modelled as a porous zone to account for the presence of the turbine.

Starting from water at rest, the wave generation process has been simulated assigning a sinusoidal motion on the left wall of the wave flume, by means of a user-defined function (UDF). The maximum

displacement of the piston type wavemaker was calculated referring to the complete first-order piston wavemaker solution, reported by Dean and Dalrymple [34], and described later in this manuscript. Smooth no-slip wall boundary conditions have been assigned to the breakwater and the flume walls, whilst the upper domain boundary is defined as a pressure outlet with zero-gauge pressure, considering the atmospheric pressure (p_a = 1.01325 bar) as the reference pressure. Air is assumed to be compressible, following the ideal-gas law, to take into account the compressibility of the air pocket inside the chamber.

2.2. The Governing Equations

The numerical approach is based on a two-dimensional unsteady CFD simulation, using the commercial code Ansys Fluent v17.0, Academic Version. The water-air interaction is taken into account by means of the volume of fluid (VOF) model. In the VOF model, two or more fluids (or phases) are not interpenetrating, and the fraction of the volume of the qth phase in a cell is called the volume fraction, $\alpha_q \in [0, 1]$. Each volume fraction is governed by its own continuity equation:

$$\frac{1}{\rho_q}\left[\frac{\partial}{\partial t}\left(\alpha_q \rho_q\right) + \nabla \cdot \left(\alpha_q \rho_q \overline{v}_q\right) = S_{\alpha_q} + \sum_{p=1}^{n}\left(\dot{m}_{pq} - \dot{m}_{qp}\right)\right], \tag{1}$$

where ρ_q is the density of the qth phase, $\overline{v}$ is the velocity vector, $\dot{m}_{qp}$ is the mass transfer from phase q to phase p, and $\dot{m}_{pq}$ is the mass transfer from phase p to phase q. The volume fraction equation will not be solved for the primary phase, standing the following constraint:

$$\sum_{q=1}^{n} \alpha_q = 1. \tag{2}$$

In our case, no source terms or mass transfer from one phase to the other are considered, hence Equation (1) is simplified as follows:

$$\frac{1}{\rho_q}\left[\frac{\partial}{\partial t}\left(\alpha_q \rho_q\right) + \nabla \cdot \left(\alpha_q \rho_q \overline{v}_q\right) = 0\right]. \tag{3}$$

The volume fraction in a cell hosting an interface between two phases is calculated by the geometric reconstruction scheme. In this approach, the interface between fluids is represented through a piecewise linear interpolation. Both air and water flow fields are assumed to be unsteady and are computed solving the governing equations, that are

- the mass conservation (or continuity) equation:

$$\frac{\partial \rho}{\partial t} + \nabla \cdot \left(\rho \overline{v}\right) = 0; \tag{4}$$

which holds both for incompressible as well as for compressible flows, and states that the mass is constant in a given system;

- the momentum balance equation:

$$\frac{\partial}{\partial t}\left(\rho \overline{v}\right) + \nabla \cdot \left(\rho \overline{v}\overline{v}\right) = -\nabla p + \nabla \cdot \left(\overline{\overline{\tau}}\right) + \rho \overline{g} + \overline{F}; \tag{5}$$

where p is the pressure, $\overline{F}$ is a source term (for instance, the one related to the porous medium) and $\overline{\overline{\tau}}$ is the stress tensor equal to

$$\overline{\overline{\tau}} = \mu\left[\left(\nabla \overline{v} + \nabla \overline{v}^T\right) - \frac{2}{3}\left(\nabla \cdot \overline{v}\right)\overline{\overline{I}}\right], \tag{6}$$

where μ is the molecular viscosity;

- the energy conservation equation:

$$\frac{\partial}{\partial t}\left[\rho\left(e+\frac{1}{2}v^2\right)\right]+\nabla\cdot\left[\rho\overline{v}\left(e+\frac{1}{2}v^2\right)\right]=\nabla\cdot\left(k_t\nabla T\right)+\nabla\cdot\left(-p\overline{v}+\overline{\overline{\tau}}\cdot\overline{v}\right)+\overline{v}\cdot\overline{F}+Q_h, \quad (7)$$

where e is the specific energy, k_t the thermal conductivity, T the temperature, Q_h a possible heat source. When a Reynolds-averaged approach is used, each generic variable ϕ can be decomposed in its averaged value (average performed over a sufficiently small time interval under unsteady flow conditions) $\overline{\phi}$, and its fluctuation ϕ'. Then, all the non-linear terms give birth to new variables, which must be opportunely modeled to resolve the problem. For instance, in the Reynolds-averaged momentum balance equation, the term $-\overline{\rho\overline{v}'\overline{v}'}$, known as the Reynolds stress tensor appears. This is a symmetric tensor and thus has six components, which must be modeled. For the closure problem, the Boussinesq hypothesis is used to relate the Reynolds stresses to the mean velocity gradients together with two transport equations for the turbulent kinetic energy k, and the specific turbulent dissipation rate ω, according to the standard $k-\omega$ turbulence model. In this work, the governing equations were discretized according to a finite volume approach, adopting a pressure-based algorithm in its implicit formulation. The semi-implicit method for pressure-linked equations (SIMPLE) scheme was used for the pressure-velocity coupling. This is a segregated algorithm that uses a relationship between velocity and pressure corrections to enforce mass conservation and to obtain the pressure field. In order to obtain the spatial discretization of the convection terms in the governing equations, we used the Green–Gauss cell-based method for the gradient evaluation and the pressure staggering option (PRESTO!) scheme for the pressure equation. The other convection-diffusion equations (e.g., momentum or energy equation) were discretised by means of the second-order upwind scheme. Regarding the temporal discretization, a time step $\Delta t = T/1000$, T being the wave period, was used. This time step size was selected to keep the courant number value much lower than 1, improving the solution convergence. A summary of the CFD simulation set up details are shown in Table 1.

Table 1. CFD simulation set up details.

Model for two-phase (water/air) interaction	Eulerian VOF
Solver	SIMPLE algorithm
Spatial discretization of Gradient	Green Gauss cell Based
Spatial discretization of pressure	PRESTO!
Spatial discretization of momentum	2nd order upwind
Spatial discretization of Volume Fraction	Geo-Reconstruct
Transient formulation	1st order implicit
Time step	1/1000 T_p
Turbolence model	$k-\omega$ - *Standard*
Reference pressure	p_a = 101,300 [Pa]

2.3. The PTO System

The part of the computational domain, indicated by a red rectangle in Figure 3, was set as a "porous zone" to model the pressure drop in the air duct due to both the presence of the Wells turbine and the minor fluid-dynamic losses. Indeed, the "porous zone" is characterized by viscous and inertial losses, which are used to reproduce the actual pressure drop in the air conduit, mainly due to the air turbine that converts the oscillating pneumatic power into mechanical power. The rationale of using a porous zone instead of the simulation of the actual duct and turbine inside, it is that the main effect that influences the fluid dynamic behaviour of the OWC is the relation between the pressure in the air chamber and the air flow in the duct. The local flow field, instead, has a limited influence. Furthermore, our simulations are 2D. The introduction of the porous medium allowed us to represent the duct without the need for respecting the equivalent cross section area. Once the cross-section of the duct has been defined in the 2D CFD model, we guarantee the same mass flow rate and the

same pressure drop by opportunely defining the porous medium coefficients. Therefore the model reproduces the relation of the air pressure drop vs. the air flow. To this purpose, the pressure drop Δp, has been subdivided into two contributions:

- Δp_t due to the turbine;
- Δp_c due to continuous and minor losses in the air conduit.

According to [7], a Wells turbine is supposed to be installed in the U-OWC breakwater of the Civitavecchia's harbor. During operation, the parameters characterizing the behavior of the turbine were recorded under several sea states. In particular, the following parameters were evaluated:

- the non-dimensional pressure drop

$$\Delta p^* = \frac{\Delta p}{\rho_a U_{tip}^2}; \tag{8}$$

- the non-dimensional flow coefficient

$$U^* = \frac{V_a}{U_{tip}}; \tag{9}$$

where V_a is the mean axial velocity in the turbine annulus, evaluated as the ratio between the volumetric flow rate Q, and the annulus are A_t:

$$V_a = \frac{Q}{A_t}, \tag{10}$$

and $U_{tip} = \omega R_{tip}$ is the blade tip speed, with ω the turbine angular speed, and R_{tip} the turbine tip radius. Introducing the hub to tip ratio $h = R_{hub}/R_{tip}$, it results

$$A_t = \pi R_{tip}^2 \left(1 - h^2\right). \tag{11}$$

The stagnation pressure drop across the Wells turbine Δp_t, is just about linearly variable with the axial flow velocity V_a, as confirmed by experiments, (e.g., [14,35]), and numerical simulations (e.g., [36–39]). Therefore, a linear relationship between the turbine parameters Δp^* and U^* is assumed in this work:

$$\Delta p^* = \frac{B_t}{2} U^*, \tag{12}$$

where B_t is the turbine damping factor. If the turbine rotates at a constant rotational speed, it produces a viscous loss for the air current.

In our CFD simulations, the viscous pressure drop Δp_v across the porous medium was set equal to the pressure drop determined by the Wells turbine Δp_t. This pressure drop can be expressed as

$$\Delta p_v = \mu_a \Delta l R_v V_p, \tag{13}$$

where R_v is the viscous coefficient, μ_a is the air molecular viscosity, Δl is the porous medium length and V_p is the air flow velocity in the porous medium. At the same time, from the definition of the turbine damping factor B_t, the turbine pressure drop Δp_t can be expressed as

$$\Delta p_t = \Delta p^* \rho_a U_{tip}^2 = \frac{B_t}{2} U^* \rho_a U_{tip}^2 = \frac{B_t}{2} \rho_a U_{tip} V_a, \tag{14}$$

hence the coefficient R_v, can be evaluated from the turbine damping factor B_t, as soon as we can relate the air flow velocity in the porous medium V_p, to the velocity across the Wells turbine V_a.

To this purpose, we have to consider that the mass flow rate through the porous medium has to be equal to the mass flow rate across the turbine:

$$\rho_a A_p V_p = \rho_a A_t V_a, \tag{15}$$

A_p being the cross section area of the porous medium, which is equal to the product of the conduit diameter and the width of the absorbing chamber (i.e., $D \times b'$). Hence

$$R_v = \frac{\Delta p_v}{\mu_a \Delta l V_p} = \frac{\Delta p_t}{\mu_a \Delta l V_p} = \frac{A_p}{A_t}\frac{B_t}{2}\frac{\rho_a U_{tip}}{\mu_a \Delta l}. \tag{16}$$

Being that the air flow is fully turbulent in the conduit, the continuous pressure losses, due to friction on the conduit walls, are calculated analytically from the Darcy–Weisback formula:

$$\Delta p_c = \frac{\rho_a F_C \Delta l V_c^2}{2D}, \tag{17}$$

where D is the diameter of the conduit, V_c is the air flow velocity in the conduit and F_c is the friction coefficient computed according to the Tsal approximation

$$F_C = 0.11\left(\frac{\varepsilon}{D} + \frac{68}{Re}\right)^{0.25}, \tag{18}$$

where ε is the wall roughness and Re is the Reynolds number.

Minor losses at the entrance and the exit of the conduit can be evaluated from

$$\Delta p_{i+o} = \frac{1}{2}\rho_a F_{i+o} V_t^2, \tag{19}$$

where F_{i+o} is the sum of the minor losses coefficients, F_i (inlet/entrance) and F_o (outlet/exit). Table 2 shows the values of these adopted coefficients.

Table 2. Parameters assumed for the computation of the continuous and minor losses.

Parameter	Value
ε [m]	3×10^{-5}
F_i	0.5
F_o	1

Both the continuous pressure losses (Δp_c) and the minor losses (Δp_{i+o}) are proportional to $\rho_a V_t^2$. Therefore, their summation is put equal to the inertial pressure drop Δp_i in the porous medium:

$$\Delta p_i = \frac{1}{2}\rho_a \Delta l R_i V_p^2, \tag{20}$$

where R_i is the inertial resistance coefficient obtained imposing $\Delta p_c + \Delta p_{i+o} = \Delta p_i$.

Finally, the total pressure drop $\Delta p_{tot} = (\Delta p_c + \Delta p_{i+o} + \Delta p_t)$, in the air duct is evaluated as the sum of the *viscous* Δp_v, and the *inertial* Δp_i, losses:

$$\Delta p_{tot} = \Delta p_v + \Delta p_i = \mu_a \Delta l R_p V_p + \frac{1}{2}\rho_a \Delta l R_i V_p^2. \tag{21}$$

3. Fluid Dynamic Analysis

3.1. The Wave Generation and Propagation

According to [40], a piston-type wavemaker starting from rest and moving sinusoidally for a given period of time t, produces a free surface displacement η, that can be expressed as

$$\eta(x,t) = \frac{2}{\pi}\int_0^\infty \frac{\tanh(kd)}{k}\cos(kx)\int_0^t U_0(\tau)\cos(\sigma(t-\tau))\,d\tau dl, \tag{22}$$

where d is the flume depth, U_0 is the horizontal velocity of the wave board, and $\sigma^2 = gk\tanh(kd)$, is the squared angular frequency of the generated waves, with $k = 2\pi/L$, being the angular wavenumber and L being the wave length. Assuming the board starts from rest at its extreme backward position, its displacement and velocity are given by

$$X(t) = -\frac{S}{2}\cos(\omega t), \tag{23}$$

$$U_0(t) = \frac{S}{2}\omega\sin(\omega t), \tag{24}$$

respectively, where S is the total horizontal stroke excursion, and ω is the angular frequency of the wave board. As reported by Huges [40], a simplified theory for plane wavemakers in shallow water was proposed by Galvin (1964), who imposed that the water displacement by the wavemaker is equal to the crest volume of the propagating wave form. Considering a piston-type wavemaker with a stroke S, along the entire water depth d, the volume of water displaced over a whole stroke is actually Sd (see Figure 4), whereas the volume of water below a wave crest is

$$\int_0^{L/2}(H/2)\sin(kx)\mathrm{d}x = \frac{H}{k}. \tag{25}$$

Equating the two volumes, we obtain

$$Sd = \frac{H}{k} = \frac{H}{2}\left(\frac{L}{2}\right)\frac{2}{\pi}, \tag{26}$$

where the factor $2/\pi$ represents the ratio between the shaded area and the area of the enclosing rectangle (see Figure 4). This equation can also be expressed as

$$\left(\frac{H}{S}\right)_{\text{piston}} = kd, \tag{27}$$

where H/S is the height-to-stroke ratio. This relationship is valid in the shallow water region, $kd < \pi/10$.

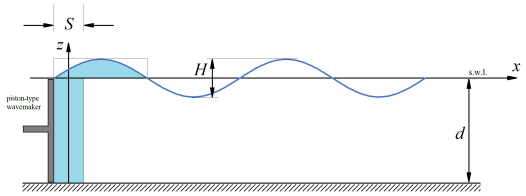

Figure 4. Sketch for the simplified shallow water piston-type wavemaker theory of Galvin.

In this work, we carried out numerical simulations assigning a sinusoidal motion to the left wall of the wave flume, in order to simulate wave trains formed by periodic regular waves. The aim is to reproduce three sea states having significant wave height H_s, and peak period characteristics T_p, typical for the location of the Civitavecchia plant: (1) significant height H_s= 2.0 m and peak period T_p = 6 s ; (2) H_s = 3.0 m, and T_p = 7.4 s; (3) H_s = 3.5 m, and T_p = 8 s (see sea state No. 4, 6 and 7 in [7], respectively). To calculate the stroke S, we have considered a periodic wave height H with a wave period $T \equiv T_p$, energetically equivalent to the significant wave height H_s, of each sea state, whilst remembering the basic relations in the theory of the sea states [41]:

$$< \eta^2(t) >= \frac{H_s^2}{16}, \tag{28}$$

and

$$< \eta^2(t) >= \sum_{i=1}^{N} \frac{1}{2} a_i^2, \tag{29}$$

being, for a monochromatic periodic wave a_i equal to $H/2$ we have:

$$H = \frac{H_s}{\sqrt{2}}. \tag{30}$$

Table 3 shows the characteristic values of the simulated wave trains and the corresponding parameters of the generated, energetically equivalent, wave trains.

Table 3. The wave trains simulated.

Wave Trains	H_s [m]	T [s]	H [m]	S [m]	U_r [−]
SS4	2.5	6.0	1.4	0.901	1.18
SS6	3.0	7.4	2.1	1.725	3.38
SS7	3.5	8.0	2.5	2.218	4.90

$U_r = HL^2/d^3$ is the Ursell number.

To test the wave generation and propagation in the flume, the values of $\eta(y,t)$ registered during the CFD simulation for the SS7 wave train, were compared with the analytical ones. Figure 5 shows the instantaneous free surface elevation along the flume, a few time instants after the beginning of the piston motion (actually, after 6 wave periods). For comparison, the analytical solution Equation (22) is superposed. As we can see, there is a good agreement between the two sets of data.

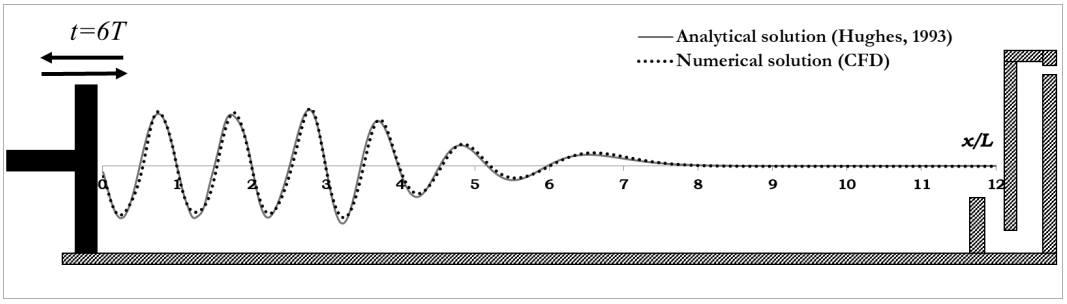

Figure 5. Free surface displacement η, as a function of relative distance x/L, where L represents the wavelength. Comparison between analytical solution (continuous line) for transient waves in a flume (Huges, 1993) and the numerical solution (dotted line) carried out by CFD simulation ($H = 2.5$ m, $T = 8$ s).

3.2. The Wave Field in Front of the Plant

The wave field in front of the absorber-breakwater is produced by the interaction between incoming waves, reflected waves and the pulsating discharge through the plant. Figure 6 shows, for the SS7 wave train, that we considered as a test, the overlapping of several snapshots of the surface waves in the flume, in which each frame is taken every $\Delta t = T/20$, during a wave period T. As we can see, the flow field in front of the U-OWC breakwater is quite different from the standing wave field in front of a vertical reflecting wall. This quasi-standing wave field is characterized by the presence of quasi-nodes, which are points where the amplitude of η is at its minimum but different from zero (as they are in the standing waves). Moreover, when the incident wave train has impacted the absorber-breakwater, the wave amplitude at the breakwater wall is smaller than in front of a vertical reflecting wall. Indeed, the amplification factor β (equal to the ratio of the wave amplitude at the U-OWC breakwater wall and H) is 0.85.

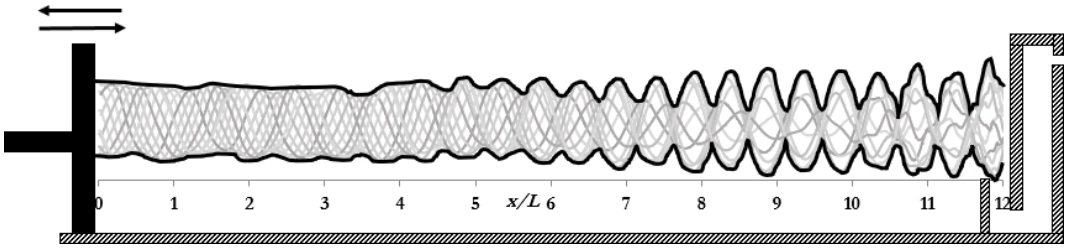

Figure 6. Overlapping of several snapshots of the flume surface during a wave period as a function of x/L. In the marked line the envelope of the quasi-standing field is represented ($H = 2.5\ m$, $T = 8\ s$). Along abscissas $4L < x < 6L$, the transition from the incoming waves and the quasi standing field is evident.

4. Analysis of the Energy Conversion Process

4.1. The Energy Flux of the Generated Waves

To verify the share of the incident wave energy captured by the U-OWC, we have calculated the mean energy flux $\overline{\Phi}$, at different vertical sections along the wave flume:

$$\overline{\Phi} = \frac{1}{T}\int_0^T \int_0^\eta \Delta p(z,t) V_x(z,t) \mathrm{d}z\mathrm{d}t, \tag{31}$$

where $\Delta p(z,t)$ is the wave pressure and $V_x(z,t)$ is the horizontal velocity. The integral was calculated numerically in 14 points (Δz = 1.35 m) from the bottom up to the maximum free surface displacement. In order to additionally check the numerical wave generation process, incident fluxes, calculated along the flume, were compared with that obtained by means of the linear wave theory:

$$\overline{\Phi}_{lwt} = \frac{1}{8}\rho g H^2 c_G, \tag{32}$$

where c_G is the wave group velocity:

$$c_G = \frac{1}{2}\sqrt{\frac{g}{k}\tanh(kd)}\left(1 + \frac{2kd}{\sinh(2kd)}\right). \tag{33}$$

The incident wave flux $\overline{\Phi}_{AA'}$, is calculated at a fixed abscissa near the wavemaker, averaged over the time interval during which a progressive wave is established. Figure 7 shows the mean energy flux of the incident waves versus the wave period T, for the three wave trains of Table 3.

As we can see, there is a reasonably good agreement, being that the maximum difference between theoretical and numerical values, corresponding to the same wave period, is about 20%. This difference is acceptable considering that Equation (32) is valid for waves of small amplitude. The wave field along the flume is unsteady in time and not homogeneous in space. Initially, we have a progressive wave train generated by the wavemaker traveling towards the U-OWC, in a flume at rest. After the impact with the breakwater wall, we have a new wave field expanding in the opposite direction and superposing on it. To analyze the energy propagation mechanism, we chose several vertical sections where the mean energy flux was evaluated (see Figure 8).

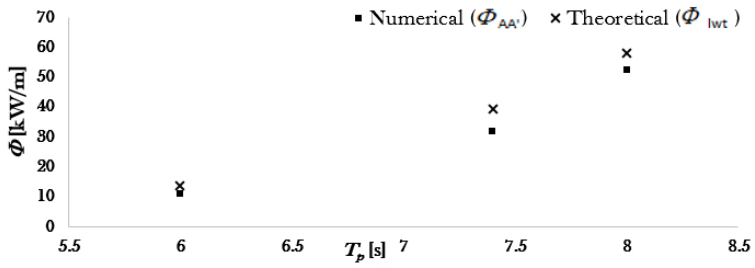

Figure 7. The mean energy flux of the incident waves. Crosses show theoretical values, calculated by Equation (32), and squares the numerical ones computed in section AA', by means of Equation (31).

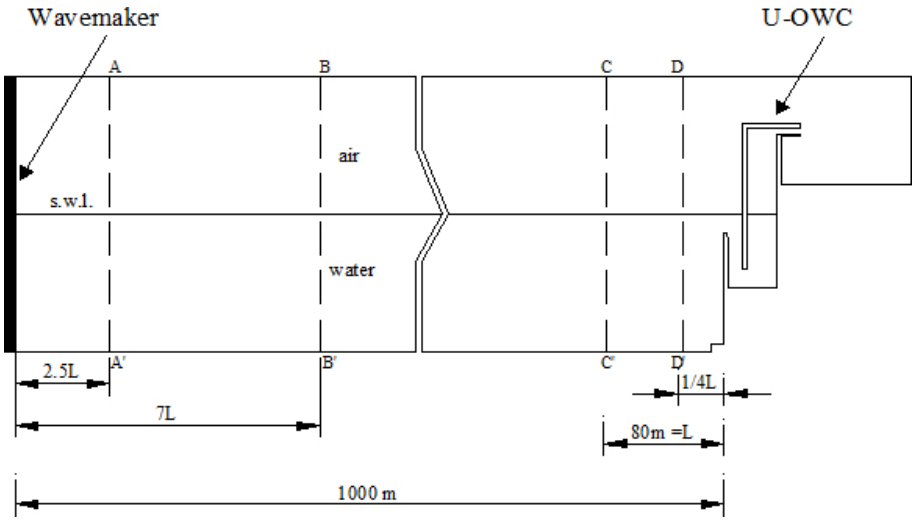

Figure 8. Vertical cross sections at different abscissas along the flume, where the energy flux is evaluated (distances, both from the wavemaker and the absorber, are referred to the wavelength L, of the wave train no. 7).

Regarding the first cross section (AA'), the nearest to the wavemaker, the instantaneous energy flux evaluated by Equation (32) is shown in Figure 9. During the time interval reproduced in abscissa, waves are periodic and progressive with H = 2.5 m, T = 8 s.

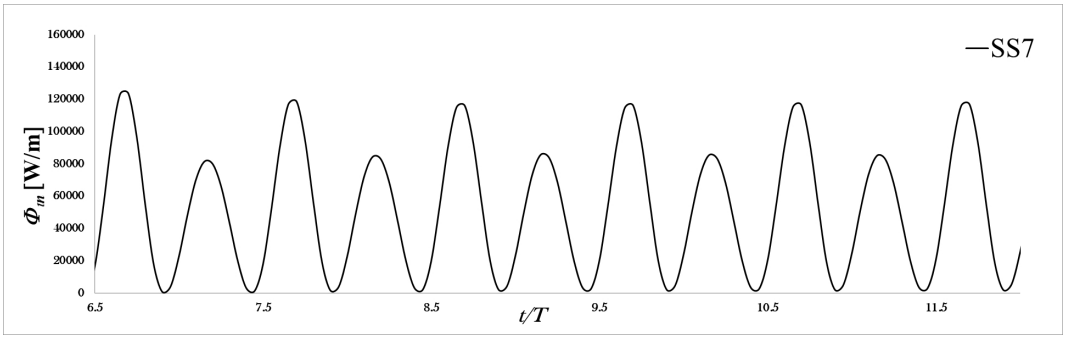

Figure 9. Instantaneous energy flux in the AA' section, placed at 2.5 L from the wavemaker of Figure 8 (H = 2.5 m, T = 8 s).

In the shown time interval (see Figure 9), the mean flux is 52.5 kW/m, 10% less than the energy flux evaluated by means of Equation (32). In this section, the energy fluxes of the incident waves for all the simulated wave trains are calculated. The second section (BB') is placed at the middle length of the computational flume, and the instantaneous energy flux is shown in Figure 10, during a time

interval when progressive waves are crossing this section. The mean energy flux in section BB' is equal to 46.5 kW/m, 11% less than in section AA'.

Hence, we can assume that the wave train further looses energy in order to travel across the entire flume length. For this reason, we can estimate that the wave energy reaching the U-OWC, $\overline{\Phi}_{in}$, can be evaluated as follows:

$$\overline{\Phi}_{in} = \overline{\Phi}_{AA'} - \left(\overline{\Phi}_{AA'} - \overline{\Phi}_{BB'}\right) \frac{(X_{DD'} - X_{AA'})}{(X_{BB'} - X_{AA'})}, \tag{34}$$

being $X_{AA'}$, $X_{BB'}$ and $X_{DD'}$ the abscissas of the vertical section AA', BB' and CC', respectively.

This is not surprising: the attenuation of the wave height along a wave flume was also registered by Dong and Huang [42]; furthermore, the damping rate of the wave height increases with the Ursell number. The damping is mainly caused by two contributions [34]: (1) the energy dissipation due to the bottom shear stress; (2) the energy losses in the irrotational part of the flow field, even if this latter contribution is much less significant with respect to the former. Finally, even a small attenuation of the wave height determines a significant energy loss, due to the quadratic dependence.

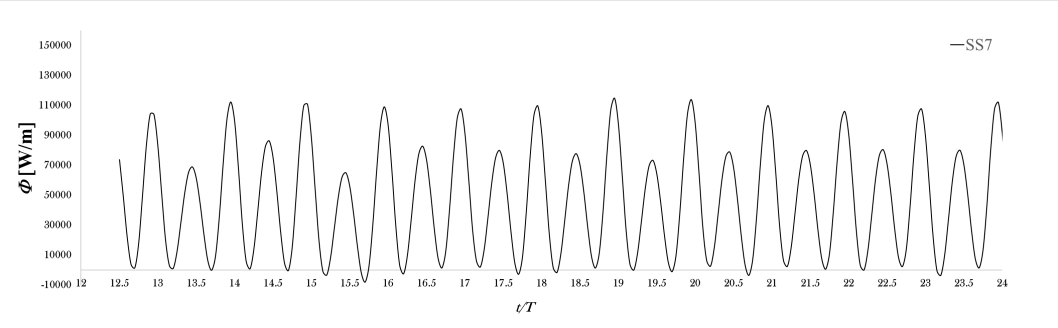

Figure 10. Instantaneous energy flux in the middle (BB') of the flume ($H = 2.5$ m, $T = 8$ s).

4.2. The Energy Flux of the Transient Waves along the Flume

Sections CC' and DD' are utilized to evaluate the energy flux of the wave field in a time interval subsequent to the impact of the incoming wave train on the absorber. In order to understand the spatial inhomogeneities of the wave field along the flume, Figure 11 shows the overlap of the free surface displacement $\eta(t)$ along the whole flume for $25T < t < 26T$, each $\Delta t = T/20$. As we can see, along a distance equal to 6 wavelengths starting from the wavemaker, the wave field is progressive. In the subsequent two wavelengths ($6\ L < x < 8\ L$), there is the transition between the waves moving towards the U-OWC and the quasi-standing field expanding in the opposite direction. In the last 3–4 wavelengths of the flume, the quasi-standing wave field is fully developed.

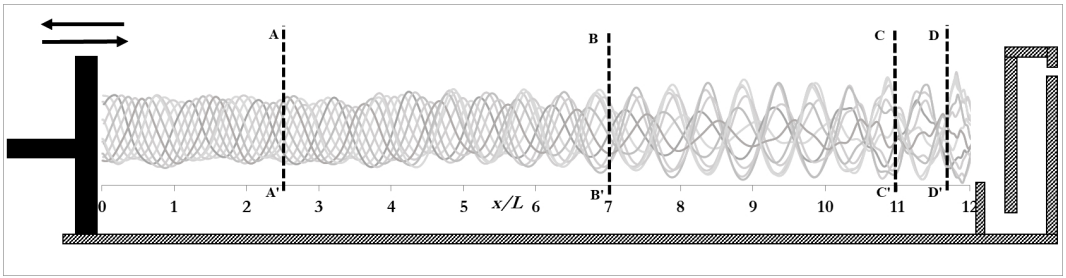

Figure 11. The envelope of the water free surface displacement from 25 T *to* 26 T, with the position of the vertical cross sections ($H = 2.5$ m, $T = 8$ s).

In the time interval shown in Figure 11, Section BB', located at $7L$ far from the wavemaker, is crossed by waves in transition between the progressive and the quasi-standing fields. Indeed, looking at the instantaneous energy flux in BB', shown in Figure 12, for the same time interval used in

Figure 11, we can identify negative energy flux, because the energy emitted by the U-OWC adds to the reflected energy in some moments, becoming bigger than the incident energy flux, as we will see in more detail in the next section.

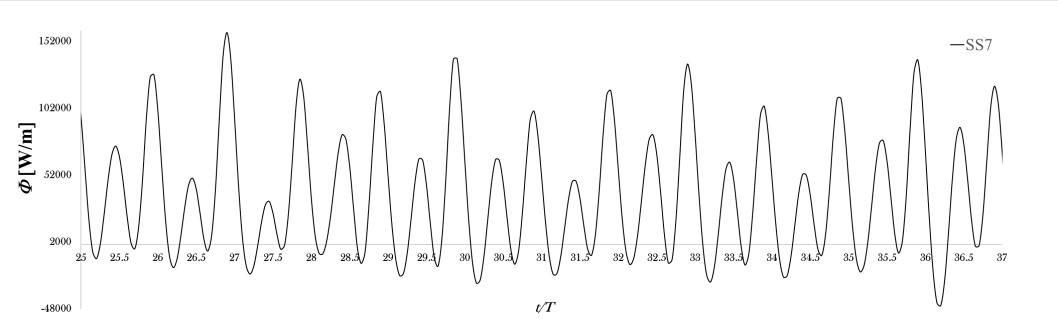

Figure 12. The instantaneous energy flux in the middle (BB') of the numerical flume, during a time period starting from $t = 25\ T$ ($H = 2.5$ m, $T = 8$ s).

In the same way, the mean energy flux in those sections closest to the plant was evaluated (CC' and DD'), and the results are summarized in Table 4.

Table 4. Mean energy flux in the six sections of Figure 8, averaged in the time intervals shown in the fourth column.

SECT.	Absolute Position x [m]	Relative Position x/L	Time Interval	$\overline{\Phi}$[kW/m]	Wave Type
AA'	200	2.5	6 T–12 T	52.5	progressive
BB'	550	6.7	12 T–23 T	46.5	progressive
BB'	550	6.7	25 T–36 T	37.0	transition zone
CC'	920	11.25	25 T–36 T	27.7	quasi-standing
DD'	980	12	25 T–36 T	29.2	quasi-standing

Note that the "wave type" column characterizes the nature of waves crossing the section indicated in the first column, during the time interval shown in the fourth column. A transient motion along the wave flume occurs near the head of both the incoming and the reflected wave trains. The first is the head of the progressive wave field generated by the wavemaker which propagates along the surface of the flume, which is initially at rest (i.e., for $3.5 \leq x/L \leq 8$ in Figure 5). The latter is the head of the reflected wave train, which superimposes the progressive wave (i.e., for $5 \leq x/L \leq 7$ in Figure 6). Progressive waves denote the periodic condition established after the passage of the head of the incoming waves or reflective waves, respectively. Summarizing, the mean energy flux of waves ($H = 2.5$ m, $T = 8$ s) $\overline{\Phi}_{AA'}$, generated by the wavemaker and flowing through section AA' is approximately equal to 52.5 kW/m. For this sea state, the estimated wave energy flux $\overline{\Phi}_{in}$ which would reach the U-OWC, is equal to 40.95 kW/m (Equation (34)). As we can see, this value is larger than the energy flux at section DD', because it represents the energy flux of the waves at section DD' in the absence of the plant, while the actual energy flux at section DD' (in the presence of the plant) is close to the energy absorbed by the plant. The energy equation applied in a control volume in front of the absorber can be written as [15]:

$$\overline{\Phi}_{in} - \overline{\Phi}_{DD'} = (\overline{E}_{qd} - \overline{E}_{in})c_r, \tag{35}$$

where $\overline{E}_{in}$ is the mean energy per unit surface of the incident waves, $\overline{E}_{qd}$ is the mean energy per unit surface of the quasi-standing wave field, and c_r is the group celerity of the quasi-standing wave field.

4.3. The Energy Flux of the Waves Close to the Absorber

Figure 13b shows the water streamlines upstream and inside the absorber breakwater. As we can see, the wave field near the plant cannot be homogeneous in space. This is due to the fact that the wave discharge is distributed along a whole vertical section (e.g., in sections AA' and BB'), while at the absorber, it is concentrated at the opening of the vertical duct (section EE' in Figure 13b). This implies that velocity streamlines lay along the exterior wall of the vertical duct, from the bottom up to its outer opening, where they abruptly turn inwards. In particular, the upper three snapshots show the time instant when the water exits the plant, occurs when there is a wave trough on the absorber wall. Conversely, during a wave crest, the flow enters the plant, as shown in the three snapshots of the lower panel.

In the vicinity of the U-OWC, every deviation of the streamlines produces large eddies and, consequently, a dissipation of energy. To quantify the mechanical energy associated with the water, air and turbine motions inside the U-OWC, we fixed three control volumes: in the U-conduit, in the plenum and in the duct containing the turbine. The first is enclosed between sections EE' and FF'; the second, between sections FF' and GG' and finally, the third, between sections GG' and HH'. Note that section FF' was chosen just below the minimum level of the air-water interface in the chamber (see Figure 13b).

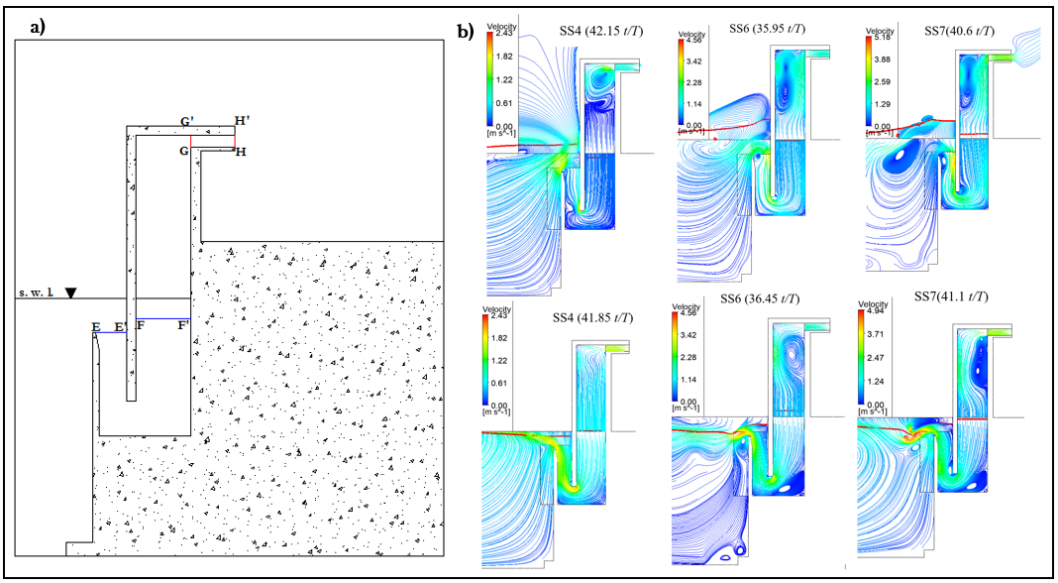

Figure 13. (**a**) Reference scheme for the evaluation of the energy flux in sections EE', FF', GG' and HH'; (**b**) streamline of velocity for each of wave train simulated.

4.4. The Captured Energy Flux

In the present work, we simulated three wave trains energetically equivalent to the sea states SS4, SS6 and SS7 reported in [7]. It is assumed that the turbine acts as a linear damper, with a damping factor $B_t = 2\Delta p^*/U^* = 4.834$, corresponding to the averaged value of a monoplane Wells turbine similar to the one designed by Curran and Gato [43]. For each sea state, the instantaneous wave energy flux absorbed by the plant $\overline{\Phi}_{abs} = \overline{\Phi}_{EE'}$, was evaluated at the horizontal cross-section on the outer opening of the vertical duct (section EE'), by multiplying the pressure fluctuation by the volumetric flow rate.

In Figure 14 the pressure fluctuation Δp, at the outer opening and the discharge Q in the plant, for the SS4 wave train ($H = 1.4$ m, $T = 6$ s) are shown.

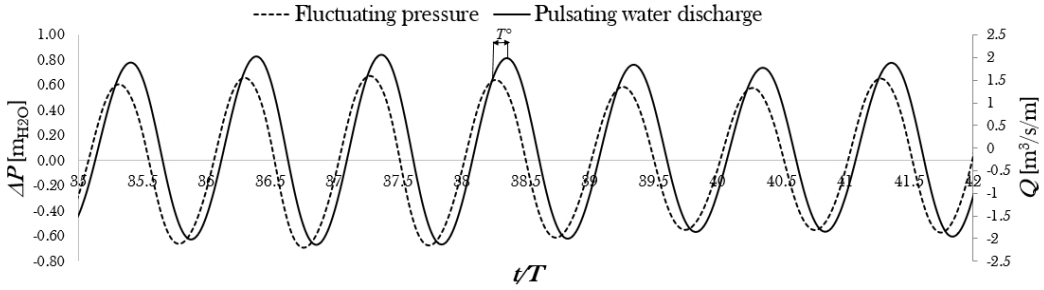

Figure 14. Pressure fluctuation Δp at the outer opening and discharge Q in the plant, as a function of t/T [The Q is positive if it enters the plant.] ($H = 1.4$ m, $T = 6$ s).

The performance of the plant is strongly affected by resonance. The resonant coefficient R, is a useful index to check how close to resonance the plant is working. It is calculated, according to [44], starting from the phase difference T° (see Figure 14), between the water discharge Q, and the fluctuating wave pressure Δp, at the outer opening of the plant (section EE') as

$$R = T^\circ/4T, \tag{36}$$

T being the wave period. R ranges in $(-1,1)$ and it is defined as positive if the pressure fluctuation anticipates the pulsating discharge, as in the case of Figure 14. Values of R lower than zero mean that the wave period is greater than the eigenperiod, whereas values larger than zero mean that the wave period is smaller than the eigenperiod. Values close to 0 mean that the plant is near to resonance.

Figure 15 shows the instantaneous energy flux absorbed by the plant for each sea state.

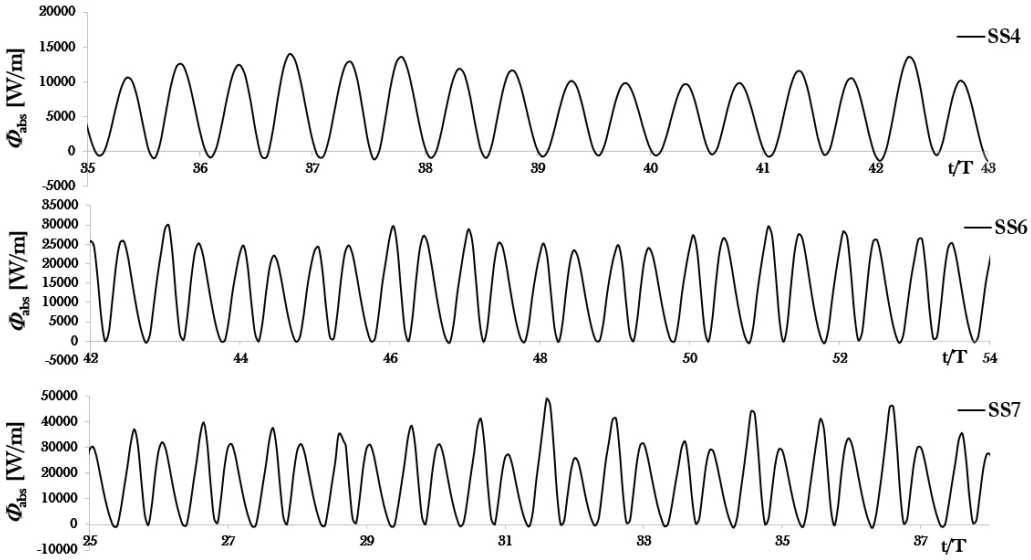

Figure 15. Time histories of the energy fluxes absorbed by the plant in the three different wave trains.

The ratio between time-averaged values of $\overline{\Phi}_{abs}$ and the estimated energy flux of incident waves $\overline{\Phi}_{in}$, represents the absorption coefficient A. For instance, for the SS7 wave train, the mean estimated energy flux $\overline{\Phi}_{in}$ of the incoming wave train is approximately equal to 40.95 kW/m whereas the time average energy flux absorbed by the plant $\overline{\Phi}_{abs}$, is about 16.45 kW/m, which is about 40.2% of the mean estimated energy flux of the incoming wave train. Analogously, for the SS4 and SS6 wave trains, the absorption coefficients A, are 66.1% and 45.7%, respectively (see Table 5).

In Table 5, the summary of this calculation is shown. As reported by [44], R quantifies the difference between the wave period and the eigenperiod of the plant and, as previous described, it is as close to zero as the wave period is close to the eigenperiod of the absorber. In the same way, the

absorption coefficient A, grows when the eigenperiod of the plant is closer to the wave period of the incident waves. However, as shown during the experiment on a small scale model of a U-OWC described by Boccotti et al. [15] (in Table 1), A is also influenced by the steepness of the incoming waves. In particular, at the same value $|R|$, A is larger the lower the steepness of waves.

Table 5. Summary of the simulations.

Wave Train	H [m]	$\overline{\Phi}_{AA'}$ [kW/m]	$\overline{\Phi}_{BB'}$ [kW/m]	$\overline{\Phi}_{in}$ [kW/m]	$\overline{\Phi}_{abs} = \overline{\Phi}_{EE'}$ [kW/m]	$A = \overline{\Phi}_{abs}/\overline{\Phi}_{in}$ [-]	R [-]	β [-]
SS4	1.4	11.05	9.6	7.9	5.23	66.1%	0.29	0.70
SS6	2.1	31.6	29.7	27.5	12.57	45.7%	-0.11	0.68
SS7	2.5	52.5	46.5	40.95	16.45	40.2%	-0.25	0.85

4.5. The Hydraulic Power on the U-Duct

Figure 16 shows, for the three simulated wave trains, the instantaneous energy flux absorbed by the U-OWC measured at the cross-section EE' (continuous line), and the energy flux transmitted to the air mass (dashed line), computed at the cross-section FF'. As we can see, the transmitted energy flux is delayed in time with respect to the instantaneous energy flux absorbed by the plant. The difference $\Phi_{EE'}(t) - \Phi_{FF'}(t)$ is equal to the time derivative of the kinetic energy inside the control volume plus the rate of energy dissipated by heat. Averaging this difference in a time interval of a length multiple of the period T, the difference between $\overline{\Phi}_{EE'}$ and $\overline{\Phi}_{FF'}$ is equal to the dissipated power, L_w (i.e., the water energy losses), being that the mean kinetic energy contained in the control volume is constant. The fluid dynamic losses of the hydraulic current flowing in the U-conduit occur whenever there is a deviation of the streamlines, that are near the outer opening of the vertical duct and near the lower edge of the exterior wall of the chamber (see Figure 13a).

Furthermore, in our CFD simulations, air was considered as an ideal gas taking into account the compressibility effects. The loss due to the air compressibility [45], L_a, was evaluated as the difference of the average energy fluxes in section FF′ and GG′ (see Figure 16) which limit the air chamber.

Focusing on the wave train SS7, the energy flowing through section EE' ($\overline{\Phi}_{EE'} = 16.45$ kW/m), is mostly used to force the water flow to move the air mass in the chamber reducing its value in section FF' $\left(\overline{\Phi}_{FF'} = 12.58 \text{ kW/m}\right)$ by 23.5%. Similarly, for the wave trains SS4 and SS6, we have obtained a reduction of the mean energy flux of 22.5% and 26.2%, respectively. As said, these reductions represent the energy losses in water.

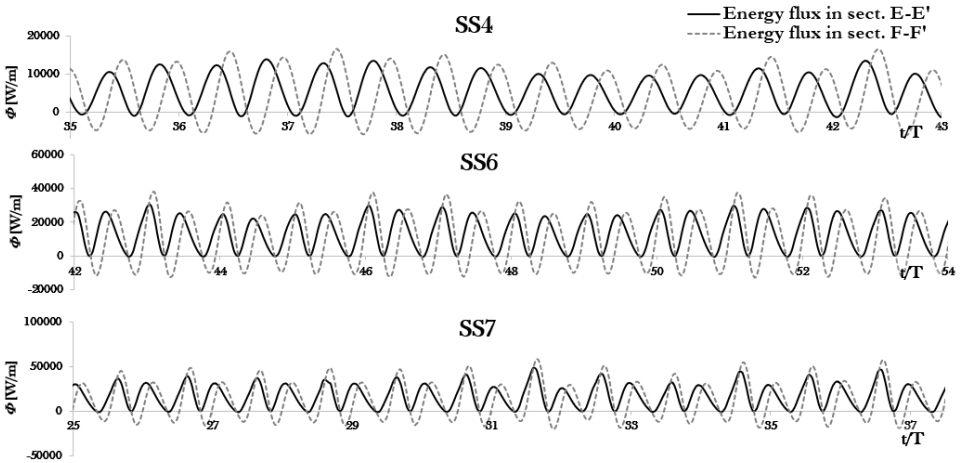

Figure 16. Time histories of the energy fluxes in sect. EE' and FF'.

4.6. The Pneumatic Power

Figure 17 shows the same analysis illustrated in Figure 16, for the control volume included between cross-sections GG' and HH', chosen to evaluate the pneumatic power absorbed in the porous medium that reproduces the behavior of the Wells turbine. The energy flux across section GG' is evaluated by multiplying the fluctuating pressure by the volumetric air flow, neglecting the internal energy due to the temperature fluctuations. The power crossing section GG' is fully absorbed in the porous medium and, therefore it is zero at section HH', where the pressure is constant and equal to the atmospheric value. The pneumatic power P_p, acting on the Wells turbine can be obtained by multiplying the energy flux $\overline{\Phi}_{GG'}$ by the width b' of one absorbing chamber, which the turbine is connected to. In other words, we have $\overline{\Phi}_{GG'} = \overline{P}_p / b'$.

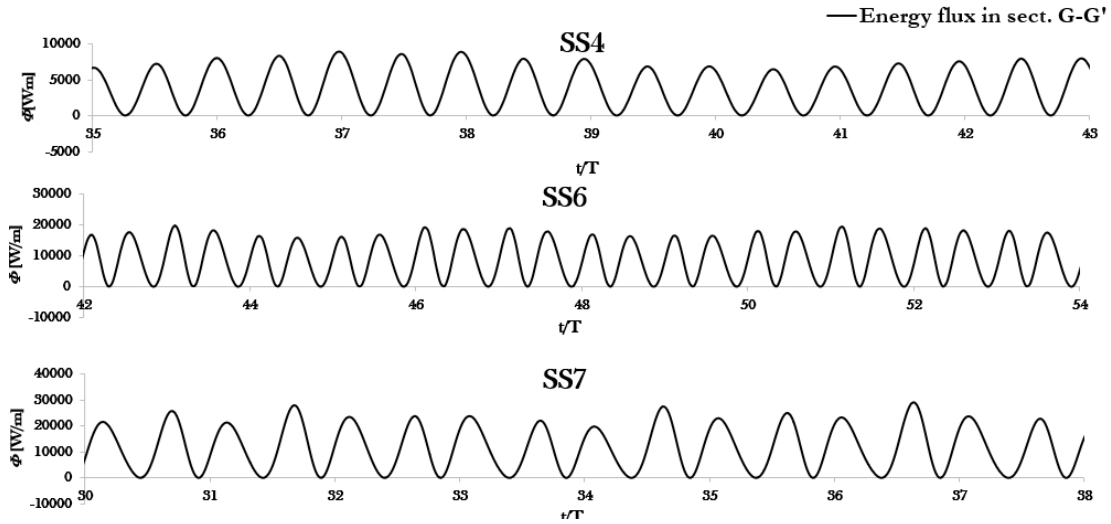

Figure 17. Time histories of the pneumatic power absorbed in the porous medium reproducing the air turbine characteristics.

4.7. The Turbine Shaft Power

In order to estimate the average shaft power, the Wells turbine installed into the U-OWC is supposed to be equivalent (in terms of non-dimensional characteristics: T^*, Δp^* and η, vs. U^*) to the monoplane studied by Curran and Gato [43].

In order to guarantee the desired R_v value, a turbine with a tip radius $R_{tip} = 0.41$ m was considered, and for each wave train the rotational speed has been opportunely modified (see Table 6).

Table 6. Viscous coefficient in the equivalent porous medium.

Wave Train	n [rpm]	R_v [1/m^2]
SS4	2129	5472×10^4
SS6	2330	5990×10^4
SS7	2608	6704×10^4

Under the previous hypothesis, the instantaneous turbine shaft power was easily computed. At each time step, the flow coefficient across the Wells turbine was evaluated by considering the mass flow rate across the equivalent porous medium (Figures 18–20). With the computed U^* (by means of a simple interpolation of the experimental data of Curran and Gato [43]) it was possible to evaluate the turbine efficiency $\eta = \eta(U^*)$, and hence the shaft power by multiplying the pneumatic power ($P_\pi = Q\Delta p$) by the efficiency η:

$$P_t = \eta_t Q \Delta p. \tag{37}$$

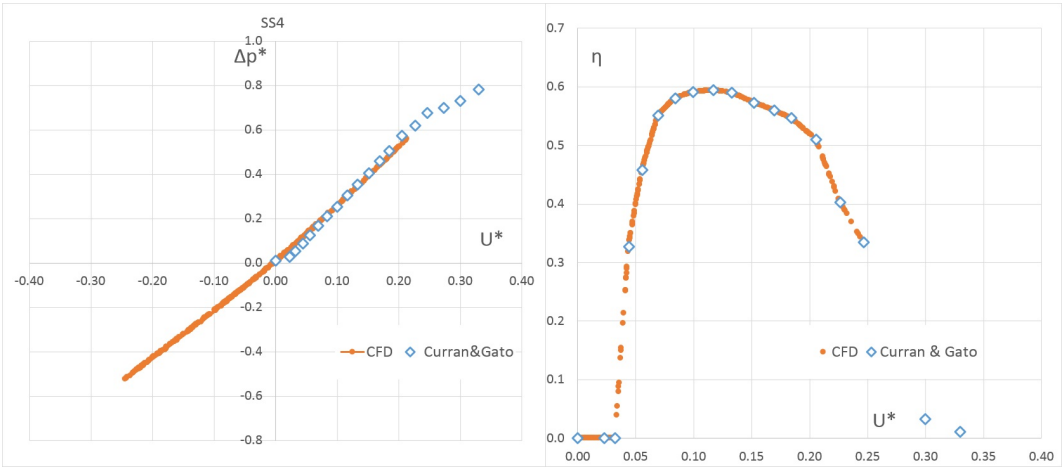

Figure 18. Equivalent characteristic curves of the Wells turbine (SS4).

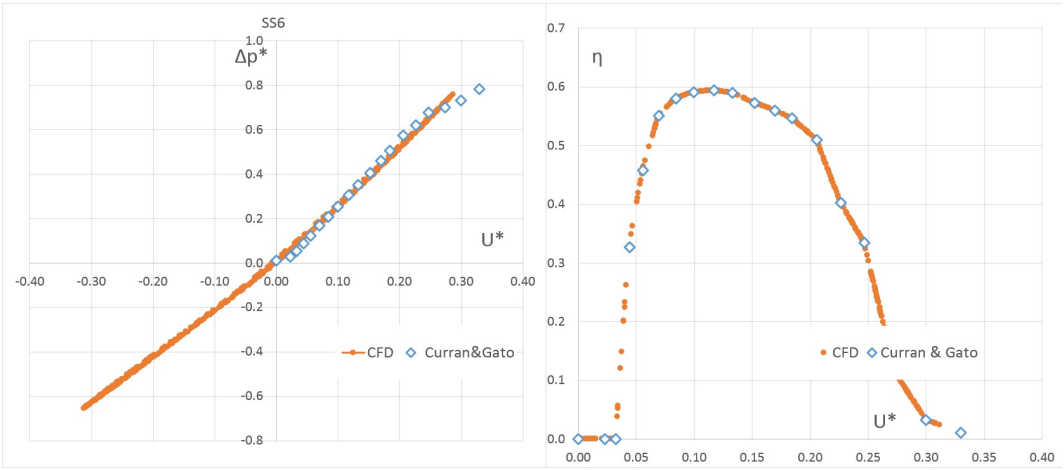

Figure 19. Equivalent characteristic curves of the Wells turbine (SS6).

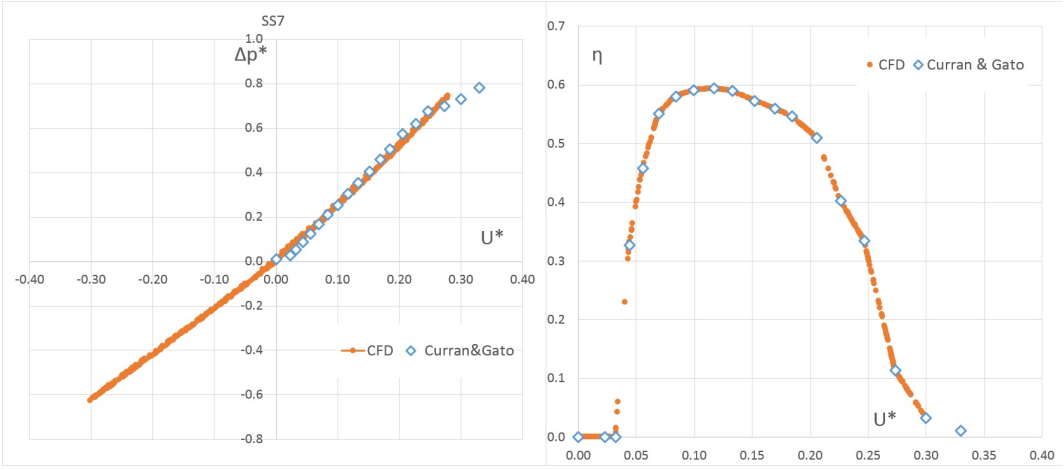

Figure 20. Equivalent characteristic curves of the Wells turbine (SS7).

Then, averaging over a finite number of periods, the average power outpt can be obtained. Table 7 summarizes the energy conversion process inside the U-OWC device starting from the average energy flux absorbed by the U-OWC, measured at the cross-section EE', $\overline{\Phi}_{EE'} = \overline{\Phi}_{abs}$, and ending with the output power of the turbine, P_t. Due to the water power losses, L_w, at the cross-section FF', the WEC experiences the first significant reduction (ranging from 22.5% for the SS4 to 26.2% for the SS6 of $\overline{\Phi}_{EE'}$). Due to the adiabatic non-isentropic thermodynamic transformations experienced cyclically by the air inside the plenum chamber, a further loss (ranging from 5.9% for the SS4 to 6.7% for the SS6 of $\overline{\Phi}_{FF'}$), indicated as L_a, reduces the average energy flux at the cross-section GG', $\overline{\Phi}_{GG'}$, which is equal to the average pneumatic power $\overline{P}_\pi/b'$. Finally, taking into account the turbine performance, it can be shown that the average turbine power output, $\overline{P}_t$, ranges from 40% for the SS6 to 48% for the SS4 of the average pneumatic power, $\overline{P}_\pi$.

Table 7. Summary of the average power and efficiency for each simulation.

Wave Train	$\overline{\Phi}_{in}$	$\overline{\Phi}_{EE'} = \overline{\Phi}_{abs}$	$\overline{\Phi}_{FF'}$	$L_w/\overline{\Phi}_{EE'}$	$\overline{\Phi}_{GG'} = \overline{P}_\pi/b'$	$L_a/\overline{\Phi}_{FF'}$	$\overline{\eta}_t$	$\overline{P}_t/b'$
-	[kW/m]	[kW/m]	[kW/m]	-	[kW/m]	-	-	[kW/m]
SS4	7.9	5.23	4.03	22.5%	3.72	5.9%	48%	2.04
SS6	27.5	12.57	9.28	26.2%	8.66	6.7%	40%	3.27
SS7	40.95	16.45	12.58	23.5%	11.79	6.3%	42%	4.67

Figure 21 shows the graphical representation of the evolution of the wave power from the generation to the turbine shaft. As we can see, part of the wave power generated by the wavemaker is dissipated during the propagation of the waves along the flume. A share of the energy flux, which reaches the plant (i.e., the incident wave power, Φ_{in}), is spent to increase the energy density of the quasi standing wave field in front of the plant and partially wasted due to hydrodynamic losses (see Equation (35)). The energy flux captured by the plant, $\Phi_{EE'}$ is partially dissipated by minor losses in the motion of the water inside the U-duct, and in the plenum chamber. The turbine shaft power P_t, is the pneumatic power P_π, multiplied by the turbine efficiency η_t.

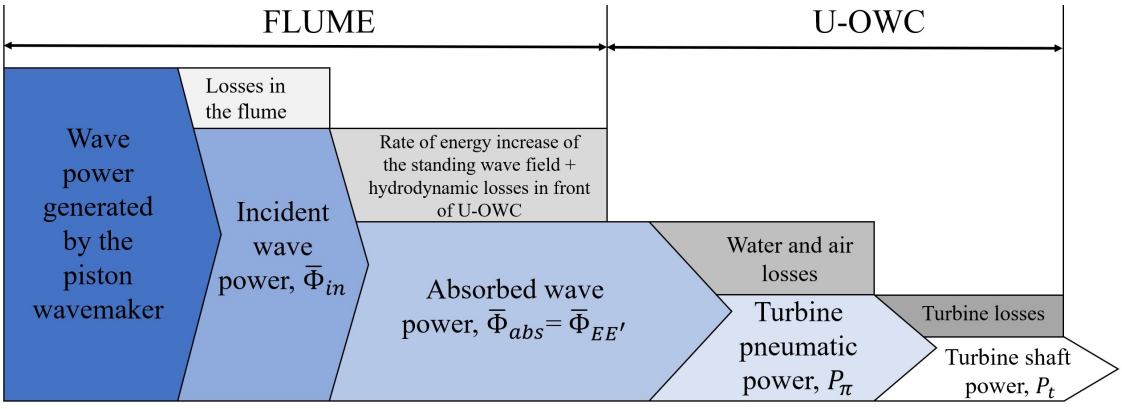

Figure 21. Evolution of the energy from the wavemaker to the Wells turbine.

5. Conclusions

A numerical experiment to investigate the energy conversion process from wave to wire of a WEC was presented. The plant belongs to the family of OWCs, even if it is different from conventional plants, due to the presence of an additional vertical duct in front of the wave beaten wall, and connected to the plenum chamber, actually forming a U-duct. Due to this specific configuration, waves cannot enter the plant; therefore, the water motion inside it is like a pipe flow. However, this solution implies both

advantages and disadvantages. An advantage is that the outer opening of the vertical duct is closer to the water surface where the pressure fluctuations are larger. However, the U-shape configuration increases the fluid dynamics of minor losses due to abrupt changes in the direction of the water motion. The paper quantifies these losses, simulating the operating conditions of a U-OWC under the action of three different periodic wave trains. The wave sizes are chosen to investigate the plant working near resonance. The PTO system is simulated using an original approach, which utilizes a porous medium in the air duct containing the turbine. The area and the pressure drop across the porous medium are set in order to have the same air discharge and pressure drop across the turbine. The results confirm this model's success at reproducing the given turbine characteristic curves. The CFD simulations were carried out by means of the commercial CFD code Ansys Fluent v.17, using a Volume of Fluid model to simulate the multiphase flow. The U-OWC breakwater installed in the Civitavecchia's harbor (Italy) was put in a 2D numerical flume. The energy conversion was analyzed, starting from the generated wave power to the turbine shaft, taking into account the energy dissipation step by step. First of all, we estimated the wave power dissipated along the 1 km flume, with the aim to quantify the actual wave energy which hits the absorber wall. This evaluation can be only carried out supposing a constant-rate energy dissipation along the flume, being that the evaluation of the incident wave energy near the plant is impossible, due to the interaction with the plant itself. Secondly, we evaluated the energy flux captured by the plant and consequently the absorbed coefficient of the plant, is that the latter is the share of the incident wave power captured by the plant. We focused our attention on the amount of energy lost from the plant entrance to the turbine duct. Analyzing the energy conversion process in-depth, for instance considering the SS7 wave train, we found that about 1/3 of the energy loss occurs in the water motion, because of the presence of large eddies at the outer opening of the vertical duct and near the lower edge of the exterior wall of the chamber. Therefore, nearly 66% of the absorbed energy is converted into pneumatic power which is made available in the turbine duct. Finally, looking at the streamlines colored by the velocity magnitude (Figure 13a), it appears evident that the shape of the plant could be optimized, in order to reduce the vortices and consequently, to reduce the energy losses in water.

Author Contributions: L.G., P.G.F.F. and M.T. wrote the paper; L.G. performed CFD analysis, got the results and draft the paper; P.G.F.F. organized the layout of the paper and discussed the hydrodynamics of the wave flume and WEC; M.T. arranged the porous medium model to represent the presence of the Wells Turbine; S.M.C. co-operated with L.G., P.G.F.F. and M.T. on the theoretical aspects concerning this topic; P.G.F.F., M.T. and S.M.C. supervised the work. All authors have read and agreed to the published version of the manuscript.

Funding: This research received no external funding.

Acknowledgments: The computing resources and the related technical support used for this work have been provided by CRESCO/ENEAGRID High Performance Computing infrastructure and its staff (G. Ponti et al., 2014 [46]). CRESCO/ENEAGRID High Performance Computing infrastructure is funded by ENEA, the Italian National Agency for New Technologies, Energy and Sustainable Economic Development and by Italian and European research programmes, see http://www.cresco.enea.it/englishforinformation. International Conference on High Performance Computing and Simulation, HPCS 2014, art. no. 6903807, 1030-1033.

Conflicts of Interest: The authors declare no conflict of interest.

Abbreviations

CFD	Computational Fluid Dynamics
OWC	Oscillating Water Column
PRESTO	Pressure staggering Option
PTO	Power Take-Off
RANS	Reynolds Averaged Navier Stokes
SIMPLE	Semi-implicit method for pressure-linked equations
S.W.L.	Still Water Level
U−OWC	U shaped Oscillating Water Column
VOF	Volume Of fluid
WEC	Wave Energy Converter

Nomenclature

a	[m]	Depth of the outer opening of the plant
A	[-]	Absorption coefficient
A_t	[m^2]	Annulus area
A_p	[m^2]	Cross section area of the porous medium
b	[m]	Width of the oscillating water column
b'	[m]	Width of one absorbing cell
B_t	[-]	Turbine damping factor
c	[m]	Length of the chamber
c_G	[m/s]	Celerity group
c_r	[m/s]	Celerity group of the quasi-standing wave field
d	[m]	Flume depth
D	[m]	Diameter of the conduit
e	[m^2/s^2]	Specific energy
E_π	[kW/m]	Pneumatic energy to the Wells turbine
$\overline{E}_{in}$	[kJ/m^2]	Mean energy per unit surface of the incident waves
$\overline{E}_{qd}$	[kJ/m^2]	Mean energy per unit surface of the quasi-standing wave field
$\overline{F}$	[N/m^3]	Source term for the porous medium
F_C	[-]	Friction coefficient
F_i	[-]	Inlet minor losses coefficients
F_{i+o}	[-]	Sum of the minor losses coefficients
F_o	[-]	Outlet minor losses coefficients
g	[m/s^2]	Gravity acceleration
h	[-]	Hub to tip ratio
H	[m]	Wave height
H_s	[m]	Significant wave height
k	[m^2/s^2]	Turbulent kinetic energy
k_t	[W/m/K]	Thermal conductivity
$k = 2\pi/L$	[rad/m]	Wave number
l	[m]	Length of the water duct
L	[m]	Wave length
L_w	[kW/m]	Water power losses
L_a	[kW/m]	Power losses in the air chamber
$\dot{m}_{qp}$	[$kg/s/m^3$]	Mass transfer from phase q to phase p
$\dot{m}_{pq}$	[$kg/s/m^3$]	Mass transfer from phase p to phase q
p	[Pa]	Pressure
p_a	[Pa]	Atmospheric pressure
P_π	[kW]	Pneumatic power
P_t	[kW]	Turbine shaft power
Q_h	[W/m^3]	Eventual heat source
Q	[m^3/s]	Volumetric flow rate
R	[-]	Resonant coefficient
Re	[-]	Reynolds number
R_i	[-]	Resistance coefficient
R_{tip}	[m]	Turbine tip radius
S	[m]	Total horizontal stroke excursion of the piston wavemaker
s	[m]	Width of the vertical duct
T°	[s]	Time shift between Δp and Q on the outer opening of the plant
T	[s]	Wave period
T	[K]	Temperature
T^*	[-]	Non dimensional torque coefficient
T_p	[s]	Peak period
t	[s]	Time

$U_r = HL^2/d^3$	[-]	Ursell number
U_0	[m/s]	Horizontal velocity of the wave board
U^*	[-]	Non dimensional flow coefficient
U_{tip}	[m/s]	Blade tip speed
$\overline{v}$	[m/s]	Velocity vector
V_a	[m/s]	Velocity across the Wells turbine
V_c	[m/s]	Velocity across the conduit
V_p	[m/s]	Air flow velocity in the porous medium
V_t	[m/s]	Air flow velocity in the conduit
α_q	[-]	Volume fraction
β	[-]	Amplification factor
Δl	[m]	Length of the porous medium
Δt	[s]	Time step
Δp_t	[Pa]	Pressure drop due to the turbine
Δp_i	[Pa]	Inertial losses
Δp_c	[Pa]	Pressure drop due to continuous and minor losses in the air duct
$\Delta p(y,t)$	[Pa]	Pressure fluctuation with respect to the hydrostatic pressure
Δp_v	[Pa]	Viscous losses
Δp^*	[-]	Non dimensional pressure drop
ε	[m]	Wall roughness
η	[m]	Free surface elevation
η_t	[-]	Turbine efficiency
$\overline{\Phi}$	[kW/m]	Mean energy flux per unit length
$\overline{\Phi}_{in}$	[kW/m]	Mean incident wave flux
$\overline{\Phi}_{lwt}$	[kW/m]	Mean incident wave flux of the linear wave theory
$\overline{\Phi}_{abs}$	[kW/m]	Mean wave energy flux absorbed by the plant
μ	[kg/(ms)]	Molecular viscosity
μ_a	[kg/(ms)]	Air molecular viscosity
ρ_q	[kg/m^3]	Density of the q^{th} phase
$-\overline{\rho \overline{v}' \overline{v}'}$	[N/m^2]	Reynolds stress tensor
σ	[rad/s]	The angular frequency of the generated waves
$\overline{\overline{\tau}}$	[N/m^2]	Stress tensor
ω	[1/s]	Specific turbulent kinetic dissipation rate
ω	[rad/s]	Turbine angular speed
ω	[rad/s]	Wave angular frequency

References

1. Falcão, A.F.d. First-generation wave power plant: Current status and R&D requirements. In Proceedings of the OMAE2003 22nd International Conference on Offshore Mechanics and Arctic Engineering, Cancun, Mexico, 8–13 June 2003.
2. Falcão, A.F.d. Wave energy utilization: A review of the technologies. *Renew. Sustain. Energy Rev.* **2010**, *14*, 899–918. [CrossRef]
3. Drew, B.; Plummer, A.R.; Sahinkaya, M.N. A review of wave energy converter technology. *Proc. Inst. Mech. Eng. Part J. Power Energy* **2009**, *223*, 887–902. [CrossRef]
4. Falnes, J. *Ocean Waves and Oscillating Systems*; Cambridge University Press: Cambridge, UK, 2002; p. 288, ISBN 0-521-01749-1.
5. Falcão, A.F.d.; Henriques, J.C.C. Oscillating-water-column wave energy converters and air turbines: A review. *Renew. Energy* **2016**, *85*, 1391–1424. [CrossRef]
6. Falcão, A.F.d.; Henriques, J.C.C.; Gato, L.M.C.; Gomes, R.P.F. Air turbine choice and optimization for floating oscillating-water-column wave energy converter. *Ocean. Eng.* **2014**, *75*, 148–156. [CrossRef]
7. Arena, F.; Fiamma, V.; Laface, V.; Malara, G.; Romolo, A.; Strati, F.M. Monitoring of the U-OWC under construction in Civitavecchia (Rome, Italy). In Proceedings of the 11th European Wave and Tidal Energy Conference (EWTEC), Nantes, France, 6–11 September 2015.

8. Otaola, E.; Garrido, A.J.; Lekube, J.; Garrido, I. A Comparative Analysis of Self-Rectifying Turbines for the Mutriku Oscillating Water Column Energy Plant. *Complexity* **2019**, 6396904. [CrossRef]
9. Lekube, J.; Garrido, A.J.; Garrido, I. Rotational Speed Optimization in Oscillating Water Column Wave Power Plants Based on Maximum Power Point Tracking. *IEEE Trans. Autom. Sci. Eng.* **2017**, *14*, 681–691. [CrossRef]
10. Available online: http://www.oceantecenergy.com/ (accessed on 5 January 2020).
11. Pereiras, B.; Lopez, I.; Castro, F.; Iglesias, G. Non-dimensional analysis for matching an impulse turbine to an OWC (oscillating water column) with an optimum energy transfer. *Energy* **2015**, *87*, 481–489. [CrossRef]
12. Boccotti, P. Comparison between a U-OWC and a conventional OWC. *Ocean Eng.* **2007**, *34*, 799–805. [CrossRef]
13. Boccotti, P. Design of breakwater for conversion of wave energy into electrical energy. *Ocean Eng.* **2012**, *51*, 106–118. [CrossRef]
14. Camporeale, S.M.; Filianoti, P.G.F. Energy conversion of OWC devices with additional vertical ducts. In Proceedings of the 27th International Conference on Offshore Mechanics and Arctic Engineering, OMAE 2008 Estoril, Estoril, Portugal, 15–20 June 2008; Volume 6, pp. 739–750.
15. Boccotti, P. Caisson breakwaters embodying an OWC with a small opening–Part I: Theory. *Ocean Eng.* **2007**, *34*, 806–819. [CrossRef]
16. Boccotti, P.; Filianoti, P.G.F.; Fiamma, V.; Arena, F. Caisson breakwaters embodying an OWC with a small opening—Part II: A small-scale field experiment. *Ocean Eng.* **2007**, *34*, 820–841. [CrossRef]
17. Torresi, M.; Scarpetta, F.; Martina, G.; Filianoti, P.G.F.; Camporeale, S.M. Numerical prediction of the natural frequency of an OscillatingWater Column operating under resonant conditions. *Int. J. Ocean Clim. Syst.* **2016**, *7*, 100–107. [CrossRef]
18. Scarpetta, F.; Gurnari, L.; Torresi, M.; Filianoti, P.G.F.; Camporeale, S.M. A CFD simulation of a full-scale U-OWC breakwater. In Proceedings of the 12th European Wave and Tidal Energy Conference (EWTEC), Cork, Ireland, 27 August–1st September 2017.
19. Filianoti, P.G.F.; Gurnari, L.; Torresi, M.; Camporeale, S.M. CFD analysis of the energy conversion process in a fixed oscillating water column (OWC) device with aWells turbine. *Energy Procedia* **2018**, *148*, 1026–1033. [CrossRef]
20. El Marjani, A.; Ruiz, F.C.; Rodriguez, M.A.; Santos, M.T.P. Numerical modelling in wave energy conversion systems. *Energy* **2008**, *33*, 1246–1253. [CrossRef]
21. Kamath, A.; Bish, H.; Arntsen, O.A. Numerical investigations of the hydrodynamics of an oscillating water column device. *Ocean Eng.* **2015**, *102*, 40–50. [CrossRef]
22. Shalbyn, M.; Elhanafi, A.; Walker, P.; Dorrel, D.G. FD modelling of a small–scalefixed multi–chamber OWC device. *Appl. Ocean Res.* **2019**, *88*, 37–47. [CrossRef]
23. Elhanafi, A.; Kim, C.J. Experimental and numerical investigation on wave height and power take–off damping effects on the hydrodynamic performance of an offshore–stationary OWC wave energy converter. *Renew. Energy* **2018**, *125*, 518–528. [CrossRef]
24. Camporeale, S.M.; Filianoti, P.G.F. A linearized model for estimating the performance of submerged resonant wave energy converters. *Renew. Energy* **2008**, *33*, 631–641.
25. Penalba, M.; Ringwood, J.V. A high-fidelity wave-to-wire model for wave energy converters. *Renew. Energy* **2019**, *134*, 367–378. [CrossRef]
26. Penalba, M.; Ringwood, J.V. A review of wave-to-wire models for wave energy converters. *Energies* **2016**, *9*, 506. [CrossRef]
27. Kelly, J.F.; Wright, W.M.D.; Sheng, W.; Sullivan, K.O. Implementation and Verification of a Wave-to-Wire Model of an Oscillating Water Column with Impulse Turbine. *IEEE Trans. Sustain. Energy* **2016**, *7*, 546–553. [CrossRef]
28. Benreguig, P.; Kelly, J.F.; Pakrashi, V.; Murphy, J. Wave-to-wire model development and validation for two OWC type wave energy converters. *Energies* **2019**, *12*, 3977. [CrossRef]
29. Torresi, M.; Saponaro, A.; Camporeale, S.M.; Fortunato, B. CFD analysis of the flow through tube banks of HRSG. In Proceedings of the ASME Turbo Expo 2008: Power for Land, Sea and Air, GT2008-51300, Berlin, Germany, 9–13 June 2008. [CrossRef]
30. Didier, E.; Conde, J.M.P.; Teixeira, P.R.F. Numerical simulation of an oscillation water column wave energy converter with and without damping. In Proceedings of the fourth International Conference on Computational Methods in Marine Engineering, Lisbon, Portugal, 28–30 September 2011; pp. 206–217.

31. Lopez, I.; Pereiras, B.; Castro, F.; Iglesias, G. Optimisation of turbine-induced damping for an OWC wave energy converter using a RANS-VOF numerical model. *Appl. Energy* **2014**, *127*, 105–114. [CrossRef]
32. He, F.; Huang, Z. Characteristics of orifices for modeling nonlinear power take-off in wave-flume tests of oscillating water column devices. *J. Zhejiang Univ. Sci.* **2017**, *18*, 329–345. [CrossRef]
33. He, F.; Li, M.; Huang, Z. An experimental study of An Experimental Study of Pile-Supported OWC-Type Breakwaters: Energy Extraction and Vortex-Induced Energy Loss. *Energies* **2016**, *9*, 540. [CrossRef]
34. Dean, R.G.; Dalrymple, R.A. *Water Wave Mechanics for Engineers and Scientists*; World Scientific Publishing Co.: Singapore, 1991—Reprinted; Prentice Hall, Inc.: Upper Saddle River, NJ, USA, 1984; pp. 170–178.
35. Torresi, M.; Camporeale, S.M.; Pascazio, G. Performance of a small prototype of a high solidity Wells turbine. In Proceedings of the 7th European Conference of Turbomachinery: Fluid Dynamics and Thermodynamics, ETC 2007, Athens, Greece, 5–9 March 2007.
36. Camporeale, S.M.; Torresi, M.; Pascazio, G.; Fortunato, B. A 3D un steady analysis of a Wells turbine in a sea-wave Energy conversion device. In Proceedings of the ASME Turbo Expo 2003, International Joint Power Generation Conference, Atlanta, Georgia, 16–19 June 2003; Volume 6.
37. Torresi, M.; Camporeale, S.M.; Strippoli, P.D.; Pascazio, G. Accurate simulation of a high solidity Wells turbine. *Renew. Energy* **2008**, *33*, 735–747. [CrossRef]
38. Torresi, M.; Camporeale, S.M.; Pascazio, G. Detailed CFD analysis of the steady flow in Wells turbine under incipient and deep stall conditions. *J. Fluid Eng.* **2009**, *131*, 071103. [CrossRef]
39. Cambuli, F.; Ghisu, T.; Virdis, I.; Puddu, P. Dynamic interaction between OWC system and Wells turbine: A comparison between CFD and lumped parameter model approaches. *Ocean Eng.* **2019**, *191*. [CrossRef]
40. Hughes, S.A. Physical Models and Laboratory Techniques in Coastal Engineering. *Adv. Ser. Ocean Eng.* **1993**, *7*, 568.
41. Boccotti, P. *Wave Mechanics for Ocean Engineering*; Amsterdam–Lausanne–New York–Oxford–Shannon–Singapore–Tokyo, an Imprint of Elsevier Oceanography Series, 64; Elsevier: Amsterdam, The Netherlands, 2000.
42. Dong, C.-M.; Huang, C.-J. Generation and propagation of water waves in a two-dimensional numerical viscous wave flume. *J. Waterw. Port Coast. Ocean Eng.* **2004**, *130*, 143–153.:3(143). [CrossRef]
43. Curran, R.; Gato, L.M.C. The energy conversion performances of several types of wells turbine designs. *Proc. Inst. Mech. Eng.* **1997**, *211*, 133. [CrossRef]
44. Boccotti, P. *Wave Mechanics and Wave Loads on Marine Structure*; Butterworth-Heinemann: Amsterdam, The Netherlands; Boston, MA, USA, 2015.
45. Sheng, W.; Alcorn, R.; Lewis, A. On thermodynamics in the primary power conversion of oscillating water column wave energy converters. *J. Renew. Sustain. Energy* **2013**, *5*, 023105. [CrossRef]
46. Ponti, G.; Palombi, F.; Abate, D.; Ambrosino, F.; Aprea, G.; Bastianelli, T.; Beone, F.; Bertini, R.; Bracco, G.; Caporicci, M.; et al. The role of medium size facilities in the HPC ecosystem: The case of the new CRESCO4 cluster integrated in the ENEAGRID infrastructure. In Proceedings of the 2014 International Conference on High Performance Computing and Simulation (HPCS 2014), Bologna, Italy, 22 September 2014; pp. 1030–1033.